Check for updates

*Special Issue Article*

WIND ENGINEERING

Wind Engineering
2019, Vol. 43(1) 64–82
© The Author(s) 2018
Article reuse guidelines:
sagepub.com/journals-permissions
DOI: 10.1177/0309524X18819898
journals.sagepub.com/home/wie
SAGE

# Study on wake-induced fatigue on wind turbine blade based on elastic actuator line model and two-dimensional finite element model

**Hang Meng[1], Fue-Sang Lien[1], Gregory Glinka[1], Li Li[2] and Jinhua Zhang[3]**

## Abstract

Atmospheric and wake turbulence have a great and immediate impact on the fatigue life of wind turbine blades. Generally speaking, wake-induced fatigue accounts for 5%–15% increase of fatigue load on the wind turbine rotor, which definitely threats the safety and economy of the whole wind farm. However, this effect is difficult to simulate which involves multi-wake interaction and fluid structure interaction. To better simulate the wake-induced fatigue on wind turbine blades, a novel elastic actuator line model is employed in this study. The elastic actuator line is a two-way coupling model, consisting of traditional actuator line model and one-dimensional implicit or explicit finite difference method beam structural model, among which the beam model takes gravitational force, aerodynamic force and centrifugal force into consideration. Large eddy simulation method in the NREL SOWFA code is employed to model the turbulence effect, including wake-induced turbulence and atmospheric turbulence. For the fatigue analysis part, the fatigue life of an NREL 5MW turbine blade subjected to upstream wind turbine wake effects is studied using the elastic actuator line model and laminate data available from Sandia Laboratory in the United States. First, the strain and stress on different composite materials, such as uniaxial carbon fibre and biaxial composite material, are recovered by using the sectional force and moment obtained with the one-dimensional beam model and two-dimensional finite element method model, namely BECAS. Second, the stress-life method, rain-flow counting method, shifted Goodman diagram (constant life diagram) and Miners rule are employed to estimate the fatigue life for different composite materials. Noticeably, elastic actuator line largely reduces the computational efforts compared with a high-resolution computational fluid dynamics model, in which each wind turbine blade is fully resolved. Both the characteristics of different composite materials and airfoil geometries will be considered during fatigue analysis. As a result, the above procedure makes the fatigue life estimation more reliable and feasible. In the case studies, the moment time series predicted by elastic actuator line and FAST are compared. The fatigue damage of NREL 5MW wind turbine under turbulent neutral atmospheric boundary layer is calculated, and the fatigue critical section is determined to be at 10.25 m section from root. Finally, in the study of two in-line turbines, the fatigue damage increase by wake flow is 16%, which is close to the results from previous studies.

## Keywords

Aeroelastic simulation, actuator line, fatigue analysis

## Introduction

Wind turbine wake is an important issue for wind farms, especially for large and compact ones, which normally causes 10%–20% power production reduction (Gaumond et al., 2014) and 5%–15% fatigue increase (Thomsen and Sørensen, 1999). Therefore, the wake effect has long been seriously considered not only in the design of the wind farm (related to power loss) (Pillai et al., 2017) but also in the design of each individual wind turbine (related to fatigue increase) (Vera-Tudela and Kühn, 2017). In recent years, there are many researches focusing on and discussing about the aforementioned wake-induced power loss numerically for micro-sitting (Nedjari et al., 2017). However, the papers concentrating on simulating wake-induced fatigue are rare to see.

[1]University of Waterloo, Waterloo, ON, Canada
[2]North China Electric Power University, Beijing, China
[3]North China University of Water Resources and Electric Power, Zhengzhou, China

**Corresponding author:**
Hang Meng, University of Waterloo, Waterloo, ON N2L 3G1, Canada.
Email: windsimu@gmail.com

In fact, as evident in some experimental papers, wake-induced fatigue was observed in the real wind farms that ranged from a small onshore wind farm including four wind turbines (Dahlberg et al., 1992) to a large offshore Vindeby wind farm (Frandsen et al., 1996) including 11 wind turbines. Similarly, wake-induced fatigue was also observed from the Danwin wind farm with 180 kW wind turbines (Dahlberg et al., 1992) to the Samsung wind farm with the modern Megawatt turbines (Kim et al., 2015). Therefore, in order to evaluate the wind turbine longevity and optimize the wind farm layout design, numerical modelling of wake-induced fatigue is required. In addition, there exists a trend that design of wind turbine blades are getting larger (Barnes et al., 2015), and the wake effect will be stronger. Thus, the fatigue issue of these turbine blades becomes even more important, because the existing composite material is supposed to bear larger stress and stress amplitudes or fatigue loading. To overcome the aforementioned fatigue damage on wind turbine blades with existing composite materials, some fatigue mitigation methods are proposed, such as bend-twist coupling blade (Stäblein et al., 2017) and active moving surface (Chen et al., 2017), which also cannot be realized and optimized without the assistance of wake-induced fatigue simulation.

Practically, the physical simulation of wake-induced fatigue is not an easy work, including transient simulation of atmospheric boundary layer (ABL) (Cortina et al., 2017), wake flow and blade structural motion (Lee et al., 2017b). In the real wind farm, the wake flow interacts with ABL, and different wakes will also interact with each other (Miao et al., 2017). Furthermore, there also exists interaction between blade structure and ABL flow with wakes. To lower the computational cost, in the existing aeroelastic codes, such as DTU HAWC2 and NREL FAST, the effect of ABL is simplified using a turbulence generator (Veers, 1988), and the wake flow is simulated with a dynamic wake meandering (DWM) model (Bayo and Parro, 2015), such as the dynamic Ainslie wake model (Göçmen et al., 2016). These simplifications are based on assumptions of presumed atmospheric turbulence spectrum, wake flow symmetry and wake superposition (Vermeer et al., 2003). These assumptions lower the capability of the aeroelastic code to predict the fatigue loading in multi-wake situation. In the recent research by NREL about the comparison among the DWM model, large eddy simulation (LES) and field data, it is found that the aeroelastic code with the DWM model greatly overpredicted the RMS (root mean square) of the fluctuating root bending moment compared with LES results and field data (Churchfield et al., 2015). Recently, in the NREL SOWFA project, researchers coupled the actuator line model with the NREL FAST code in their LES framework, which, to the authors' best knowledge, is the first attempt to simulate the ABL flow, wake flows and blade structural motion simultaneously in the wind farm scale (Lee et al., 2017a).

Following this concept, the 'elastic actuator line' (EAL) model is proposed in this article, which is a two-way coupling model combining the actuator line model with the finite difference elastic beam model. Compared with the modal approach used in FAST 7 (Jonkman and Buhl, 2005), this elastic beam model can be established without modal analysis and modal truncation. And compared with the FEM formulation in recently published FAST 8 and HAWC2 (Vorpahl et al., 2014), the finite difference formulation of the proposed EAL makes it easy to implement. Another feature of our proposed EAL is that a two-dimensional cross-sectional analysis based on DTU BECAS (Blasques, 2015) is added in the fatigue analysis part to recover the stress and strain on each section of a wind turbine blade from the moment and force resultants of the aforementioned elastic beam model. As a result, the stress-based method can be used rather than the moment-based method employed in the NREL research paper, by which the fatigue damage of different composite materials can be calculated separately. This is because different composite materials have different fatigue damage resistance and different longevities.

The main body of present article can be divided into three parts, including the methodology, case study and conclusions. In the first part, the EAL model, two-dimensional cross-sectional model and fatigue analysis method will be presented. In the second part, the comparison between the proposed EAL and the combination of AL and FAST (in SOWFA) is carried out in terms of the bending moment prediction and fatigue damage of a single NREL 5MW wind turbine. And the wake-induced fatigue will be studied for two in-line NREL 5MW wind turbines. In the third part, the conclusions are made.

## Methodology

Roughly speaking, our methodology to estimate the fatigue damage of a wind turbine blade can be split into three parts. In the first part, the two-way coupling between the actuator line model and one-dimensional beam model is made to simulate the moment and force resultant time histories at each blade section, which is the EAL model. Next the stress and strain at each point on the cross section are recovered by using two-dimensional finite element analysis BECAS. Finally, the rainflow counting algorithm and shifted Goodman diagram will be employed to predict the fatigue damage from the stress history. The flowchart of methodology is shown in Figure 1.

This section can be divided into three subsections. In the first subsection, the EAL model including one-dimensional beam model and actuator line model will be introduced, which involves theoretical model discretized in both its explicit and implicit numerical forms. In the second part, the two-dimensional cross-sectional model (BECAS) will be briefly explained. Finally, the fatigue analysis method will be presented.

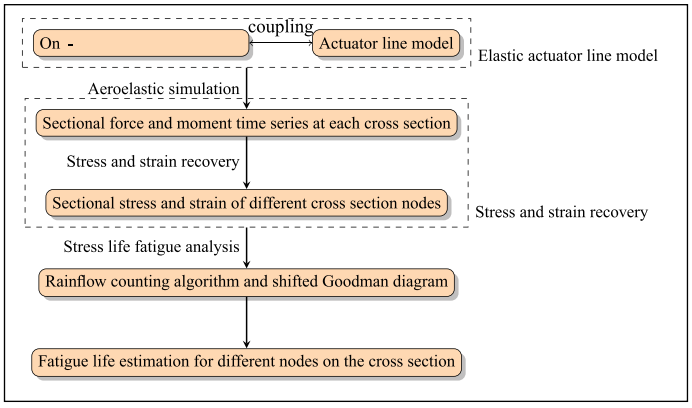


**Figure 1.** Flowchart of methodology.

## *EAL model*

In the EAL model, the aerodynamic force is predicted by the actuator line model. Similar to the conventional actuator line, the local aerodynamic force is calculated by using local velocity ( $U_{n,local}$ and $U_{t,local}$ ) and two-dimensional airfoil data ( $C_l - \alpha$ and $C_d - \alpha$ ). Contrary to the conventional actuator line model, for each actuator element of EAL, the local inflow angle $\phi$ is calculated by the following equation

$$\tan\phi = \frac{U_{n,local} + U_{e0}}{U_{t,local} + \Omega r + U_{e1}} \tag{1}$$

In the above equation, the Ω is the rotational speed of rotor and the $r$ is the radial distance (direction 2 shown in Figure 2(a)) along wind turbine blade (at root, $r = 0$ ). $U_{e0}$ and $U_{e1}$ are the vibration-induced velocity in directions 0 and 1 defined in Figure 2(a).

Similar to the conventional actuator line model, the calculated aerodynamic forces of actuator elements act as the body forces in the flow field. To avoid singularity, the body forces are smeared by the Gaussian function below (Sørensen and Shen, 2002)

$$\vec{f}_\epsilon = \frac{1}{\epsilon^3 \pi^{\frac{3}{2}}} e^{-\left(\frac{d}{\epsilon}\right)^2} \vec{f}_{2D} \tag{2}$$

$$d^2 = |\vec{x} - \vec{x}_0|^2 \tag{3}$$

In this equation, $\vec{f}_\epsilon$ is the smeared body force in the flow field. $\epsilon$ is a parameter which controls the smearing sphere radius. $\vec{f}_{2D}$ is the calculated aerodynamic force of each actuator element. $\vec{x}_0$ is the position of an actuator element, $\vec{x}$ is the position of a control point in the computational fluid dynamics (CFD) mesh and $d$ is the distance between them.

To calculate the aforementioned vibration-induced velocity in equation (1), the structural motion of wind turbine blades needs to be modelled. In this study, an one-dimensional beam model based on Euler–Bernoulli assumption is proposed to simulate the structural motion. On the basis of the defined coordinate system in Figure 2(a), the governing equations of the beam model in terms of displacement $(\vec{q})$ are presented in the following equations

$$\begin{aligned} &\rho_s(r)\frac{\partial^2 q_0}{\partial t^2} + \rho_s(r)c\frac{\partial q_0}{\partial t} + \frac{\partial^2}{\partial r^2}\left(EI_{00}(r)\frac{\partial^2 q_0}{\partial r^2} + EI_{01}\frac{\partial^2 q_1}{\partial r^2}\right) \\ &- \frac{\partial}{\partial r}\left(N(r)\frac{\partial q_0}{\partial r}\right) - f_{2D,0} - \left(\rho_s(r)\vec{g}\right)_0 = 0 \end{aligned} \tag{4}$$

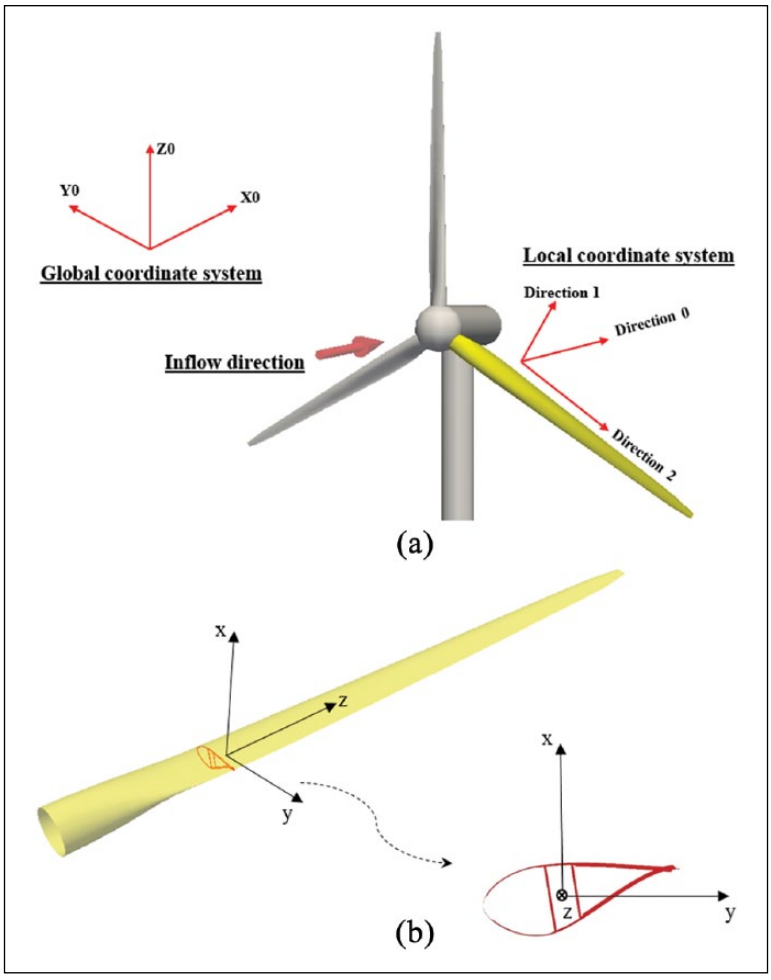


**Figure 2.** Coordinate systems used in this study: (a) Coordinate system of one-dimensional beam model in EAL and (b) coordinate system of two-dimensional cross-sectional model.

$$\rho_s(r)\frac{\partial^2 q_1}{\partial t^2}+\rho_s(r)c\frac{\partial q_1}{\partial t}+\frac{\partial^2}{\partial r^2}\left(EI_{11}(r)\frac{\partial^2 q_1}{\partial r^2}+EI_{10}\frac{\partial^2 q_0}{\partial r^2}\right)-\frac{\partial}{\partial r}\left(N(r)\frac{\partial q_1}{\partial r}\right)-f_{2D,1}-\left(\rho_s(r)\vec{g}\right)_1=0 \tag{5}$$

where

$$EI_{00}=EI_e-\left(EI_e-EI_f\right)\cos^2\theta \tag{6}$$

$$EI_{11}=EI_f-\left(EI_e-EI_f\right)\cos^2\theta \tag{7}$$

$$EI_{01}=EI_{10}=\sin 2\theta\left(\frac{EI_e-EI_f}{2}\right) \tag{8}$$

$$N(r)=\int_r^R \rho_s(r)\Omega^2 r dr \tag{9}$$

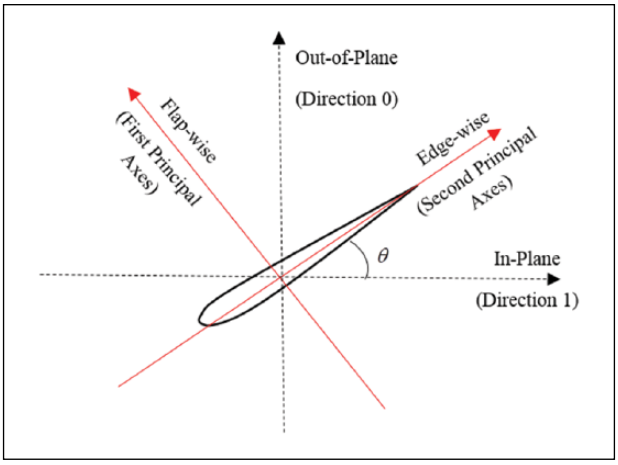


**Figure 3.** The illustration of structural twist angle.

In the above equations, $r$ represents the radial distance (in direction 2), and $R$ is the rotor radius; $q_0$ and $q_1$ are two components (in direction 0 and 1) of beam node displacements at a distance $r$ from root. Normally, the cross-sectional stiffness is calculated under the principal coordinate system, in which the two deflection components (flapwise and edgewise) are decoupled. In the above equations, $EI_f$ and $EI_e$ are flapwise and edgewise stiffness at each blade section. And there exists a twist angle $\theta$ between the principal coordinate system (flapwise and edgewise) and aforementioned local coordinate system defined in Figure 2(a). Due to this twist angle, a transformation of stiffness from the principal coordinate system to the local coordinate system is needed (equations (6) and (7)), and thus equations (4) and (5) are coupled together. The twist angle is shown in Figure 3.

To solve the governing equations above, we face two problems. The first one is that the variables in the above governing equations are displacements instead of the velocity of motion and bending moment that we need in aeroelastic simulation and fatigue analysis. The second one is that there exists higher order (i.e. higher than second order) terms in equations (4) and (5), which makes the numerical scheme complicate to discretize. To solve two aforementioned problems, a transformed formulation of equations (4) and (5) is proposed in this study, which are given below

$$\rho_s(r)\frac{\partial V_0}{\partial t}+\rho_s(r)V_0+\frac{\partial^2 M_0}{\partial r^2}-\frac{\partial S_0}{\partial r}-f_{2D,0}-\left(\rho_s(r)\vec{g}\right)_0=0 \tag{10}$$

$$\rho_s(r)\frac{\partial V_1}{\partial t}+\rho_s(r)V_1+\frac{\partial^2 M_1}{\partial r^2}-\frac{\partial S_1}{\partial r}-f_{2D,1}-\left(\rho_s(r)\vec{g}\right)_1=0 \tag{11}$$

$$\frac{\partial M_0}{\partial t}=EI_{00}\frac{\partial^2 V_0}{\partial r^2}+EI_{01}(r)\frac{\partial^2 V_1}{\partial r^2} \tag{12}$$

$$\frac{\partial M_1}{\partial t}=EI_{11}\frac{\partial^2 V_1}{\partial r^2}+EI_{10}(r)\frac{\partial^2 V_0}{\partial r^2} \tag{13}$$

$$\frac{\partial S_0}{\partial t}=N(r)\frac{\partial V_0}{\partial r} \tag{14}$$

$$\frac{\partial S_1}{\partial t} = N(r)\frac{\partial V_1}{\partial r} \tag{15}$$

By using the above transformed equations, the variables of governing equations are changed from displacements to the velocity of motion and bending moment that are needed in aeroelastic simulation, and the highest order of derivative is reduced to up to second order. Obviously, the above equations do not have analytical solution, because the $f_{2D,0}$ and $f_{2D,1}$ are numerical values from the actuator line model. As a result, in the next stage, we will discuss how to solve the above equations numerically. First, an explicit method is employed for its simplicity

$$\frac{V_{0,i}^{n+1}-V_{0,i}^{n}}{\Delta t}+cV_{0,i}^{n+1} = -\frac{1}{\rho_{s,i}}\frac{\left(\delta M_0\right)_i^n}{\Delta r^2} + \frac{1}{\rho_{s,i}}\frac{\left(\delta S_0\right)_i^n}{\Delta r} + \frac{f_{2D,0,j}^n}{\rho_{s,i}} + \left(\vec{g}_i^n\right)_0 \tag{16}$$

$$\frac{V_{1,i}^{n+1}-V_{1,i}^{n}}{\Delta t}+cV_{1,i}^{n+1} = -\frac{1}{\rho_{s,i}}\frac{\left(\delta M_1\right)_i^n}{\Delta r^2} + \frac{1}{\rho_{s,i}}\frac{\left(\delta S_1\right)_i^n}{\Delta r} + \frac{f_{2D,1,j}^n}{\rho_{s,i}} + \left(\vec{g}_i^n\right)_1 \tag{17}$$

$$\frac{M_{0,i}^{n+1}-M_{0,i}^{n}}{\Delta t} = \left(EI_{00}\right)_i\frac{\left(\delta^2 V_0\right)_i^{n+1}}{\Delta r^2} + \left(EI_{01}\right)_i\frac{\left(\delta^2 V_1\right)_i^{n+1}}{\Delta r^2} \tag{18}$$

$$\frac{M_{1,i}^{n+1}-M_{1,i}^{n}}{\Delta t} = \left(EI_{11}\right)_i\frac{\left(\delta^2 V_1\right)_i^{n+1}}{\Delta r^2} + \left(EI_{10}\right)_i\frac{\left(\delta^2 V_0\right)_i^{n+1}}{\Delta r^2} \tag{19}$$

$$\frac{S_{0,i}^{n+1}-S_{0,i}^{n}}{\Delta t} = N_i\frac{\left(\delta V_0\right)_i^{n+1}}{\Delta r} \tag{20}$$

$$\frac{S_{1,i}^{n+1}-S_{1,i}^{n}}{\Delta t} = N_i\frac{\left(\delta V_1\right)_i^{n+1}}{\Delta r} \tag{21}$$

$$N_i = \sum_{j=i}^{N}\rho_{s,j}\Omega^2 r_j \Delta r \tag{22}$$

The solution to the equations above is straightforward because of its explicit form. First, equations (16) and (17) are solved to calculate the $V_{0,i}^{n+1}$ and $V_{1,i}^{n+1}$. Here $\delta$ is the forward difference scheme, and $\delta^2$ is the central difference scheme. Second, the calculated $V_0$ and $V_1$ are substituted to equations (18)–(21). Although this method is easy to implement and efficient, it still has its limitations in terms of allowable time step. The largest time step to guarantee the stability of equations (16)–(21) is shown below

$$\Delta t \le \sqrt{\frac{\rho_s}{EI}}\frac{\Delta r^2}{2} \tag{23}$$

To remove the limitation of time step, the implicit discretized equations are derived as shown in the following equations

$$\rho_{s,i}\frac{V_{0,i}^{n+1}-V_{0,i}^{n}}{\Delta t}+cV_{0,i}^{n+1}=-\frac{\left(\delta^2 M_0\right)_i^{n+1}+\left(\delta^2 M_0\right)_j^{n}}{2\Delta r^2}+\frac{\left(\delta S_0\right)_i^{n}}{2\Delta r}+\frac{f_{2D,0,j}^{n}}{\rho_{s,i}}+\left(g_i^n\right)_0 \tag{24}$$

$$\rho_{s,i}\frac{V_{1,i}^{n+1}-V_{1,i}^{n}}{\Delta t}+cV_{1,i}^{n+1}=-\frac{\left(\delta^2 M_1\right)_i^{n+1}+\left(\delta^2 M_1\right)_j^{n}}{2\Delta r^2}+\frac{\left(\delta S_1\right)_i^{n}}{2\Delta r}+\frac{f_{2D,1,j}^{n}}{\rho_{s,i}}+\left(g_i^n\right)_1 \tag{25}$$

$$\frac{M_{0,i}^{n+1}-M_{0,i}^{n}}{\Delta t}=\left(EI_{00}\right)_i\frac{\left(\delta^2 V_0\right)_i^{n+1}+\left(\delta^2 V_0\right)_j^{n}}{2\Delta r^2}+\left(EI_{01}\right)_i\frac{\left(\delta^2 V_1\right)_i^{n+1}+\left(\delta^2 V\right)_j^{n}}{2\Delta r^2} \tag{26}$$

$$\frac{M_{1,i}^{n+1}-M_{1,i}^{n}}{\Delta t}=\left(EI_{11}\right)_i\frac{\left(\delta^2 V_1\right)_i^{n+1}+\left(\delta^2 V_1\right)_i^{n+1}}{2\Delta r^2}+\left(EI_{10}\right)_i\frac{\left(\delta^2 V_0\right)_i^{n+1}+\left(\delta^2 V_0\right)_i^{n+1}}{2\Delta r^2} \tag{27}$$

$$\frac{S_{0,i}^{n+1}-S_{0,i}^{n}}{\Delta t}=N_i\frac{\left(\delta V_0\right)_i^{n+1}+\left(\delta V_0\right)_j^{n}}{4\Delta r} \tag{28}$$

$$\frac{S_{1,i}^{n+1}-S_{1,i}^{n}}{\Delta t}=N_i\frac{\left(\delta V_1\right)_i^{n+1}+\left(\delta V_1\right)_j^{n}}{4\Delta r} \tag{29}$$

Here $\delta$ and $\delta^2$ are all central difference schemes. If we further introduce variable $\vec{p}=[V_0 \quad V_1 \quad M_0 \quad M_1]^T$, the above equations can be represented in the following matrix equations

$$-\underset{(4\times4)}{\mathbf{A}_i}\ \vec{p}_{i+1}+\underset{(4\times4)}{\mathbf{B}_i}\ \vec{p}_i-\underset{(4\times4)}{\mathbf{C}_i}\ \vec{p}_{i-1}=\vec{d}_i \tag{30}$$

$$\underset{(4\times4)}{\mathbf{A}_i}=\begin{bmatrix} 0 & 0 & -\dfrac{\Delta t}{2\Delta r^2\rho_{s,i}} & 0 \\ 0 & 0 & 0 & -\dfrac{\Delta t}{2\Delta r^2\rho_{s,i}} \\ EI_{00,i}\dfrac{\Delta t}{2\Delta r^2} & EI_{01,i}\dfrac{\Delta t}{2\Delta r^2} & 0 & 0 \\ EI_{10,i}\dfrac{\Delta t}{2\Delta r^2} & EI_{11,i}\dfrac{\Delta t}{2\Delta r^2} & 0 & 0 \end{bmatrix} \tag{31}$$

where

$$\underset{(4\times4)}{\mathbf{B}_i}=\begin{bmatrix} 1 & 0 & -\dfrac{\Delta t}{\Delta r^2\rho_{s,i}} & 0 \\ 0 & 1 & 0 & -\dfrac{\Delta t}{\Delta r^2\rho_{s,i}} \\ EI_{00,i}\dfrac{\Delta t}{\Delta r^2} & EI_{01,i}\dfrac{\Delta t}{\Delta r^2} & 1 & 0 \\ EI_{10,i}\dfrac{\Delta t}{\Delta r^2} & EI_{11,i}\dfrac{\Delta t}{\Delta r^2} & 0 & 1 \end{bmatrix} \tag{32}$$

$$\underset{(4\times4)}{\mathbf{C}_i}=\underset{(4\times4)}{\mathbf{A}_i} \tag{33}$$

$$\vec{d}_i=\begin{bmatrix} \dfrac{f^n_{2D,0,j}}{\rho_{s,i}}+\left(\vec{g}^n_i\right)_0-\dfrac{\Delta t}{2\Delta r^2}\dfrac{1}{\rho_{s,i}}\left(M^n_{0,j-1}-2M^n_{0,j}+M^n_{0,j+1}-\dfrac{\Delta t}{2\Delta r}\dfrac{1}{\rho_{s,i}}\left(S^n_{0,j-1}-S^n_{0,j+1}\right)+V^n_{0,j}\right) \\ \dfrac{f^n_{2D,1,j}}{\rho_{s,i}}+\left(\vec{g}^n_i\right)_1-\dfrac{\Delta t}{2\Delta r^2}\dfrac{1}{\rho_{s,i}}\left(M^n_{1,j-1}-2M^n_{1,j}+M^n_{1,j+1}-\dfrac{\Delta t}{2\Delta r}\dfrac{1}{\rho_{s,i}}\left(S^n_{1,j-1}-S^n_{1,j+1}\right)+V^n_{1,j}\right) \\ M^n_{0,j}+EI_{00,i}\dfrac{\Delta t}{2\Delta r^2}\left(V^n_{0,j-1}-2V^n_{0,j}+V^n_{0,j+1}\right)+EI_{01}\dfrac{\Delta t}{2\Delta r^2}\left(V^n_{1,j-1}-2V^n_{1,j}+V^n_{1,j+1}\right) \\ M^n_{1,j}+EI_{11,i}\dfrac{\Delta t}{2\Delta r^2}\left(V^n_{1,j-1}-2V^n_{1,j}+V^n_{1,j+1}\right)+EI_{00,i}\dfrac{\Delta t}{2\Delta r^2}\left(V^n_{0,j-1}-2V^n_{0,j}+V^n_{0,j+1}\right) \end{bmatrix} \tag{34}$$

Similar to the finite element method (FEM), the above matrice equations are for the local beam element. These equations can then be assembled as a global matrix. In contrast to the FEM, shape functions are not required.

### *Two-dimensional sectional analysis model*

The fatigue analysis is normally based on the stress or strain history of the material. For the composite materials used in wind turbine industry, different materials might have different fatigue resistance characteristics. As a result, the stress

or strain history of each cross-sectional point should be recovered from the bending moment history predicted by the above EAL model and, thus, the cross-sectional analysis is required. In this study, the DTU cross-sectional code BECAS (Blasques et al., 2013) is employed to perform this analysis. In BECAS, the displacement of a point on the cross section is described as the superposition of a rigid body motion $\vec{v}$ and warping displacement $\vec{g}$. The strain of each element that we need is related to the generalized Timoshenko strain $\vec{\psi}$ from rigid body motion and the warping displacement $\vec{g}$. For two-dimensional FEM, the warping displacements $\vec{g}$ can be discretized as

$$\vec{g}(x, y, z) = \sum_i \mathbf{N}_i(x, y)\vec{u}(x_i, y_i, z) \tag{35}$$

For each FEM node, $\mathbf{N}_i$ is a $3\times 3$ matrix. An assumption is adopted here that there is a linear relation between cross-sectional force resultants $\vec{F}$ and the nodal warping displacement $\vec{u}_n$ and generalized strain $\vec{\psi}$ and their first derivatives

$$\begin{aligned} \underset{(n_d\times 1)}{\vec{u}_n} &= \underset{(n_d\times 6)}{\mathbf{X}}\underset{(6\times 1)}{\vec{F}} & \underset{(6\times 1)}{\vec{\psi}} &= \underset{(6\times 6)}{\mathbf{Y}}\underset{(6\times 1)}{\vec{F}} \\ \underset{(n_d\times 1)}{\frac{\partial \vec{u}_n}{\partial z}} &= \underset{(n_d\times 6)}{\frac{\partial \mathbf{X}}{\partial z}}\underset{(6\times 1)}{\vec{F}} & \underset{(6\times 1)}{\frac{\partial \vec{\psi}}{\partial z}} &= \underset{(6\times 6)}{\frac{\partial \mathbf{Y}}{\partial z}}\underset{(6\times 1)}{\vec{F}} \end{aligned} \tag{36}$$

The governing equations on the cross section of a wind turbine blade are established through the equilibrium of internal and external virtual work. Combing the four relations in equation (36), the equilibrium equation is derived to be two matrice equations in terms of $\mathbf{X}$, $\mathbf{Y}$, $\partial\mathbf{X}/\partial z$ and $\partial\mathbf{Y}/\partial z$. The definitions of the parameters in equations (37) and (38) can be found in Appendix 1

$$\begin{bmatrix} \underset{(n_d\times n_d)}{\mathbf{E}} & \underset{(n_d\times 6)}{\mathbf{R}} & \underset{(n_d\times 6)}{\mathbf{D}} \\ \underset{(6\times n_d)}{\mathbf{R}^T} & \underset{(6\times 6)}{\mathbf{A}} & \underset{(6\times 6)}{\mathbf{0}} \\ \underset{(6\times n_d)}{\mathbf{D}^T} & \underset{(6\times 6)}{\mathbf{0}} & \underset{(6\times 6)}{\mathbf{0}} \end{bmatrix} \begin{bmatrix} \underset{(n_d\times 6)}{\frac{\partial \mathbf{X}}{\partial z}} \\ \underset{(6\times 6)}{\frac{\partial \mathbf{Y}}{\partial z}} \\ \underset{(6\times 6)}{\mathbf{\Lambda}_1} \end{bmatrix} = \begin{bmatrix} \underset{(n_d\times 6)}{\mathbf{0}} \\ \underset{(6\times 6)}{\mathbf{T}_r^T} \\ \underset{(6\times 6)}{\mathbf{0}} \end{bmatrix} \tag{37}$$

$$\begin{bmatrix} \underset{(n_d\times n_d)}{\mathbf{E}} & \underset{(n_d\times 6)}{\mathbf{R}} & \underset{(n_d\times 6)}{\mathbf{D}} \\ \underset{(6\times n_d)}{\mathbf{R}^T} & \underset{(6\times 6)}{\mathbf{A}} & \underset{(6\times 6)}{\mathbf{0}} \\ \underset{(6\times n_d)}{\mathbf{D}^T} & \underset{(6\times 6)}{\mathbf{0}} & \underset{(6\times 6)}{\mathbf{0}} \end{bmatrix} \begin{bmatrix} \underset{(n_d\times 6)}{\mathbf{X}} \\ \underset{(6\times 6)}{\mathbf{Y}} \\ \underset{(6\times 6)}{\mathbf{\Lambda}_2} \end{bmatrix} =$$

$$\begin{bmatrix} \underset{(n_d\times n_d)}{(\mathbf{C}-\mathbf{C}^T)} & \underset{(n_d\times 6)}{\mathbf{L}} \\ \underset{(6\times n_d)}{\mathbf{L}^T} & \underset{(6\times 6)}{\mathbf{0}} \\ \underset{(6\times n_d)}{\mathbf{0}} & \underset{(6\times 6)}{\mathbf{0}} \end{bmatrix} \begin{bmatrix} \underset{(n_d\times 6)}{\frac{\partial \mathbf{X}}{\partial z}} \\ \underset{(6\times 6)}{\frac{\partial \mathbf{Y}}{\partial z}} \end{bmatrix} + \begin{bmatrix} \underset{(n_d\times 6)}{\mathbf{0}} \\ \underset{(6\times 6)}{\mathbf{I}} \\ \underset{(6\times 6)}{\mathbf{0}} \end{bmatrix} \tag{38}$$

And there is a relationship between strain and the sectional force and moment. Therefore, the model strain on the cross section can be expressed by the above $\mathbf{X}$ and $\mathbf{Y}$.

$$\underset{(6\times1)}{\epsilon_n} = \underset{(6\times3)}{\mathbf{S}}\underset{(3\times6)}{\mathbf{Z}}\underset{(6\times6)}{\mathbf{Y}_n}\underset{(6\times1)}{\vec{F}} + \underset{(6\times3)}{\mathbf{B}}\underset{(3\times3)}{\mathbf{N}_i}\underset{(3\times6)}{\mathbf{X}_n}\underset{(6\times1)}{\vec{F}} + \underset{(6\times3)}{\mathbf{S}}\underset{(3\times3)}{\mathbf{N}_i}\underset{(3\times6)}{\left(\frac{\partial \mathbf{X}}{\partial z}\right)_n}\underset{(6\times1)}{\vec{F}} \tag{39}$$

### Fatigue analysis

The fatigue analysis in this study is based on Miner's rule. The basic assumption of Miner's rule is that the damage can be accumulated linearly and independently

$$D = \sum_i \frac{1}{N\left(\sigma_{a,i}, \sigma_{m,i}\right)} \tag{40}$$

In the above equation, $D$ represents the total fatigue damage of the material and $i$ indicates the stress cycle index. And $N$ is the number of cycles to failure. $\sigma_{a,i}$ and $\sigma_{m,i}$ are the stress amplitude and mean stress, respectively. By combining the $S-N$ curve and constant life diagram (shifted Goodman relationship), the following equation can be derived to calculate the number of cycles to failure $N$ (GL, 2010)

$$N\left(\sigma_{a,i}, \sigma_{m,i}\right) = \left[\frac{\sigma_T + |\sigma_C| - 2|\gamma_{M_a}\sigma_{m,i} - \sigma_T + |\sigma_C||}{2\frac{\gamma_{M_b}}{C_{1b}}\sigma_{a,i}}\right]^m \tag{41}$$

In this equation, $\sigma_T$ and $\sigma_C$ are the ultimate tension and compression strength, respectively. $\gamma_{M_a}$ and $\gamma_{M_b}$ are safety factors for mean stress and stress amplitude. And $\gamma_{M_b}$ can be calculated by the following equation

$$\gamma_{M_b} = \gamma_{M_0}\prod_i C_{ib} \quad (i = 1,2,3,4,5) \tag{42}$$

or

$$\frac{\gamma_{M_b}}{C_{1b}} = \gamma_{M_0}\prod_i C_{ib} \quad (i = 2,3,4,5) \tag{43}$$

In the above equations, $C_{ib}$ represents the safety factor in terms of temperature effect, material fabrication effect and so on. The detailed values for $C_{ib}$ will be introduced in the following section in terms of the materials for the NREL 5MW turbine blade. And $\gamma_{M0}$ equals 1.35. The specific values for other parameters will be introduced in the following case study.

## Case study

In this section, three numerical cases are carried out to estimate the fatigue damage of single and two in-line NREL 5MW wind turbine blades. The comparison between NREL FAST and the present EAL model will be made. Then, the fatigue damage of each material at the critical section are analysed through the moment time series from the EAL model. And the 'weak point' of the existing NREL 5MW blade will be uncovered. Finally, the fatigue damage of upstream and

**Table 1.** Structural properties of NREL 5MW turbine blade.

| Material | EUD | TRIAX | BIAX | CUD |
|---|---|---|---|---|
| $E_x$ (Pa) | 4.18e10 | 2.77e10 | 1.36e10 | 1.145e11 |
| $E_y$ (Pa) | 1.4e10 | 1.365e10 | 1.33e10 | 8.39e9 |
| $E_z$ (Pa) | 1.4e10 | 1.365e10 | 1.33e10 | 8.39e9 |
| $G_{xy}$ (Pa) | 2.63e9 | 7.2e9 | 1.18e10 | 5.99e9 |
| $G_{yz}$ (Pa) | 2.63e9 | 7.2e9 | 1.18e10 | 5.99e9 |
| $G_{xz}$ (Pa) | 2.63e9 | 7.2e9 | 1.18e10 | 5.99e9 |
| $\nu$ | 0.28 | 0.39 | 0.49 | 0.27 |
| $\rho$(kg/m$^3$) | 1920 | 1780 | 1780 | 1220 |

**Table 2.** Safety factors for different materials.

| Material | $\gamma_{M_a}$ | $C_{2b}$ | $C_{3b}$ | $C_{4b}$ | $C_{5b}$ | m |
|---|---|---|---|---|---|---|
| EUD | 2.65 | 1.1 | 1.0 | 1.1 | 1.2 | 10 |
| TRIAX | 2.65 | 1.1 | 1.2 | 1.1 | 1.2 | 10 |
| BIAX | 2.65 | 1.1 | 1.2 | 1.1 | 1.2 | 10 |
| CUD | 2.65 | 1.1 | 1.0 | 1.1 | 1.2 | 14 |

**Table 3.** Thickness and strength of different materials (each ply).

| Material | Thickness (mm) | $\sigma_T$ (MPa) | $\sigma_C$ (MPa) |
|---|---|---|---|
| EUD | 0.47 | 793.05 | −542.49 |
| TRIAX fibre | 0.94 | 700 | −700 |
| BIAX fibre | 1 | 144 | −213 |
| CUD | 0.47 | 1546 | −1047 |

downstream turbines will be compared to study the wake-induced fatigue. The fluid part is simulated by using the NREL SOWFA code.

NREL 5MW turbine blade is used in this study as a baseline model, and the structural property data are available from the Sandia laboratory. From the Sandia report (Resor, 2013), it can be seen that the NREL 5MW turbine blade is mainly made of four composite materials, including E-LT-5500(EUD), SNL (TRIAX), Saertex (BIAX) and Carbon fibre (CUD). The properties of these four materials, fatigue properties and safety factors are given in Tables 1 to 3. The geometry of the blade is shown in Figure 2(b).

First, the simulation is carried out under a steady wind condition (5 m/s) to study the numerical models proposed in the 'Methodology' section. In this simulation, the standard $k-\varepsilon$ turbulence model is employed, and the out-of-plane and in-plane moments (the coordinate system is defined in Figure 2(a)) obtained FAST, the explicit EAL model and implicit EAL model are compared. The results are shown in Figure 4(a) to (c) (oop is for direction 0, and ip is for direction 1).

In Figure 4, it can be found that the FAST result and explicit EAL result are close to each other. And at the same time step (5e-4s), the moments of explicit and implicit EAL models are almost the same. As mentioned in the second section, the implicit model is proposed to overcome the limitation of time step in the explicit model. As a result, the time step is increased 10 times higher from 5e-4s to 5e-3s for the implicit model. From the results, it can be seen that the simulated moment time series do not change with the increased time step. As a result, in the following simulations, the implicit EAL model is employed instead of the explicit EAL model.

Next, the simulation under atmospheric turbulent boundary layer is carried out by using FAST and EAL model. The wind speed at hub height is around 10 m/s. The time step is 0.01 s, and the simulation time is around 100 s. The simulated flow field (at 90 s) is presented in Figure 5.

From Figure 5, we can see that the meandering wake occurs inside the turbulent ABL (in neutral) and the wake flow with velocity deficit persisting for a long distance downstream. And the simulated moment time series of EAL and FAST are compared with each other in Figure 6. It is obvious that the simulated in-plane moments of these two models are very close to each other. The simulated out-of-plane moments of these two models are on the same order of magnitude, but there still exists some discrepancies between them. We further compare the power spectrum density (PSD) of the

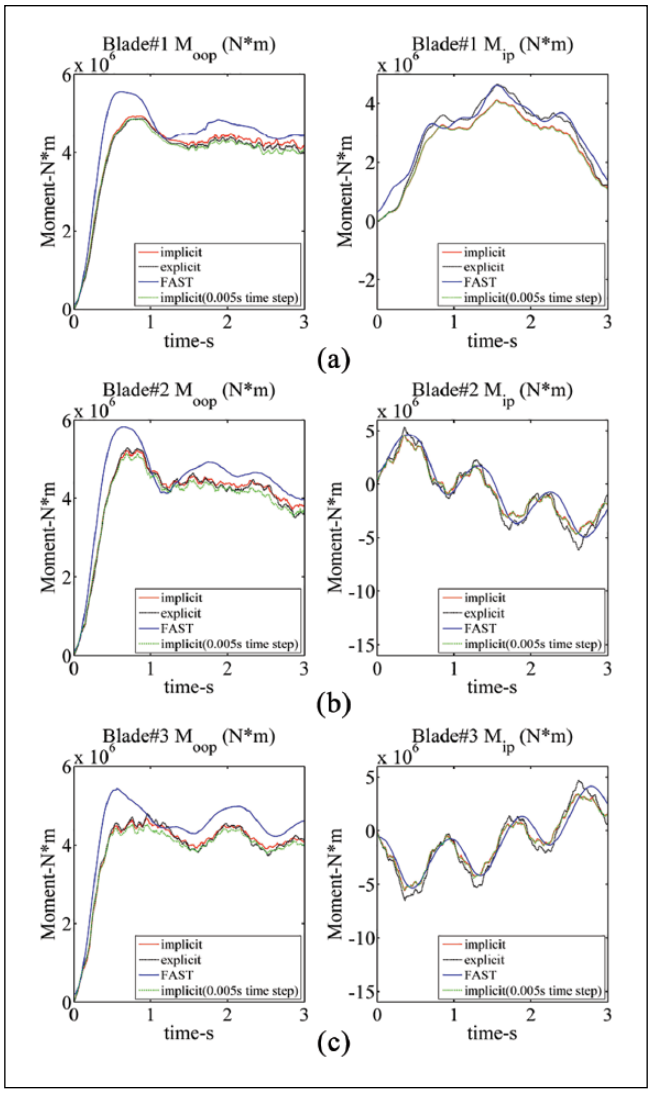


**Figure 4.** Comparison between EAL and FAST in terms of bending moments: (a) Comparison between FAST, implicit EAL, implicit EAL with a larger time step and explicit EAL (Blade 1); (b) comparison between FAST, implicit EAL, implicit EAL with a larger time step and explicit EAL (Blade 2); and (c) comparison between FAST, implicit EAL, implicit EAL with a larger time step and explicit EAL (Blade 3).

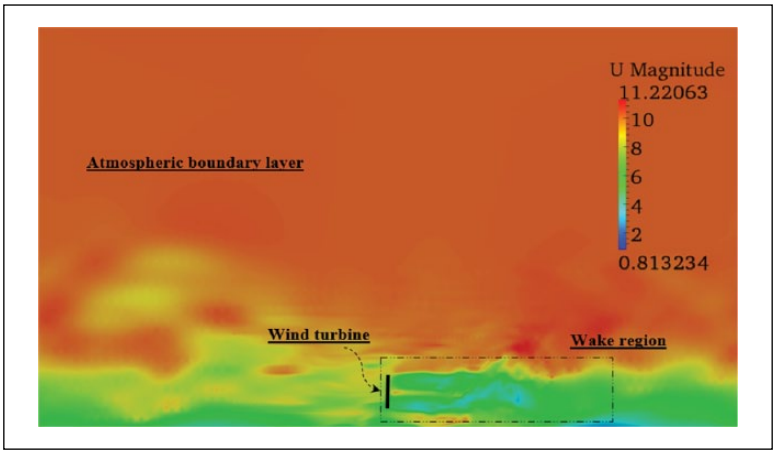


**Figure 5.** Simulated atmospheric flow and wake flow (m/s).

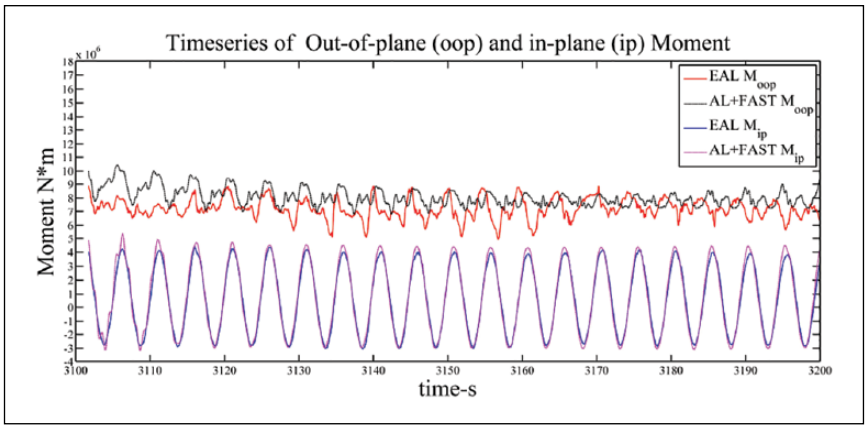


**Figure 6.** The comparison between the results of EAL model and FAST in terms of bending moments.

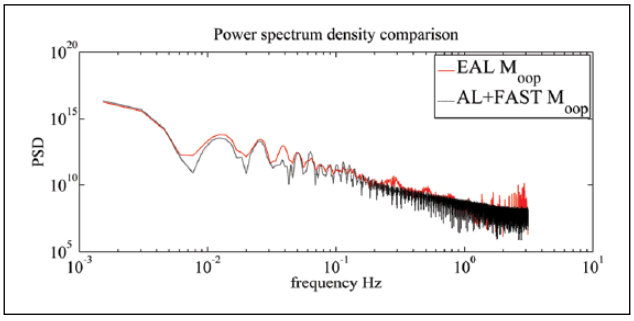


**Figure 7.** The comparison between EAL and FAST in terms of bending moment PSD.

out-of-plane moments shown in Figure 7, and it is found that they have a good agreement in the low frequency region in terms of PSD. In other words, they have similar low frequency fluctuations, which are critical to the fatigue damage.

Next, the fatigue damage at the root of the blade is calculated by using equations (40) and (41). It should be mentioned here that only TRIAX material is used at root. The fatigue damage from EAL and FAST are compared with each other in Figure 8(a) and (b). It can be seen that the fatigue damage distribution of these two models are very similar, but the calculated fatigue damage of FAST is slightly higher. The stress time series of the point with largest fatigue damage is shown in Figure 9. There is no obvious large discrepancy between them. The difference of fatigue damage value between EAL and FAST is caused by the exponential relationship between fatigue damage and stress amplitude. Although their peak values are different, they are still on the same order of magnitude. In FAST, the fatigue damage is calculated by the moment time series at root based on a moment-based fatigue analysis method. In this study, the stress life method is employed, and it will be presented in the following simulation to show that the critical section of fatigue is not always the blade root.

By using EAL, the moment time series at different cross sections can be simulated, which are shown in Figure 10(a) and (b). For out-of-plane moment, its mean value and amplitude of moment are decreasing along the radial distance (0–56.375 m, 5.125 m each section). As for the in-plane moment, the moment amplitude is also reducing from root to tip. As a result, the highest fatigue damage most likely occurs at the root because of the largest moment amplitude. Furthermore, in Table 4, the order of magnitude of fatigue damage for different materials is calculated along the blade. We can find that EUD is the most vulnerable material for the NREL 5MW turbine blade.

Then we further estimate the fatigue damage at different sections, from which it can be seen that the fatigue critical section of fatigue is between 9 and 10.25 m (from root to tip) (Figure 11). Since the airfoil at 9 m is not a standard airfoil, we mainly analyse the fatigue damage of EUD and TRIAX at 10.25 m section, which is shown in Figure 12(a) and (b). From these two figures, the location with largest fatigue damage is found to be at the trailing edge of the airfoil. We can find a fatigue damage concentration zone at this location, where the stress also concentrates because of the geometry. As mentioned above, EUD is the most vulnerable material, which is used in the reinforcement section of the airfoil and will first break down. And then the tip of the airfoil trailing edge will break, which is made of TRIAX material. When this

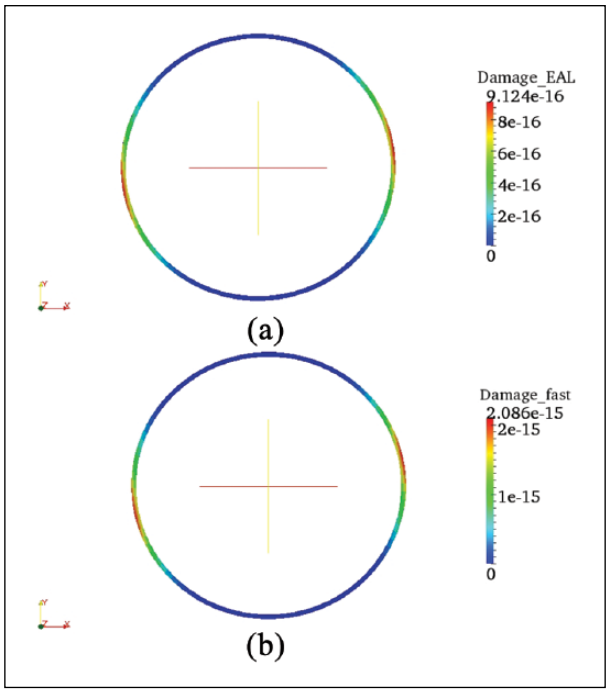


**Figure 8.** Comparison between EAL and FAST in terms of the fatigue damage at root: (a) Calculated fatigue damage at root by EAL and (b) calculated fatigue damage at root by FAST.

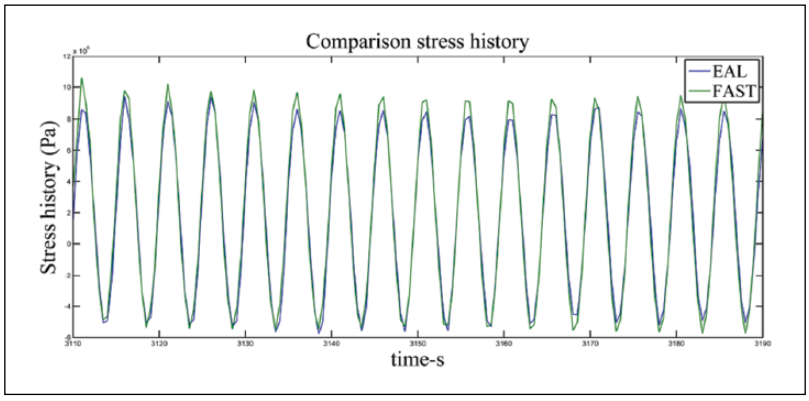


**Figure 9.** The stress time series of the largest fatigue damage point (EAL and FAST).

failure happens, the upper surface and lower surface of the airfoil will debond. And the crack will further propagate from this location to the tip and root of wind turbine blade.

Finally, the fatigue damage of two in-line NREL 5MW turbines in the same atmospheric condition is calculated to study the fatigue damage increase induced by wake. The distance between these two turbines is 200 m. The simulated flow field is shown in Figure 13. From this figure, it can be seen that the velocity deficit increases compared with the single turbine case. The fatigue damage at the fatigue critical section and critical material (i.e. EUD) of the upstream and downstream turbines are shown in Figure 14(a) and (b). From the contour colour-map, the fatigue damage of the downstream turbine blade increases by 16% compared with the upstream turbine, which coincides with the results from the previous research article (Thomsen and Sørensen, 1999).

## Conclusion

In this study, the EAL model is proposed to accomplish the aeroelastic simulation of wind turbines under atmospheric condition. The EAL is a combination of actuator line model and one-dimensional beam model. The governing equations

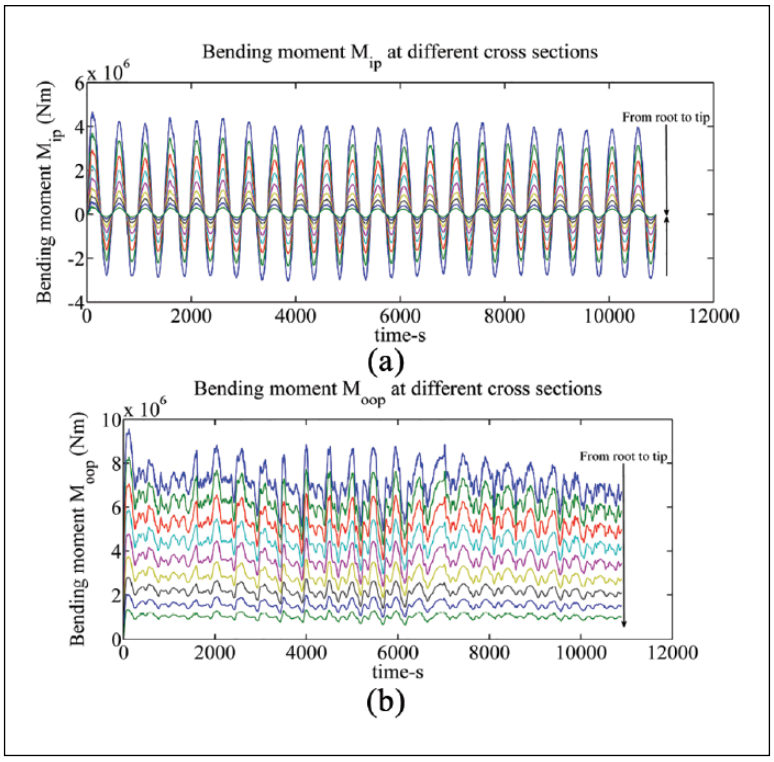


**Figure 10.** Bending moment time series at each blade section: (a) In-plane moment time series at different blade sections and (b) out-of-plane moment time series at different blade sections.

**Table 4.** The order of magnitude of fatigue damage for different materials.

| Material | EUD | TRIAX | BIAX | CUD |
|---|---|---|---|---|
| *Damge* | 1e-6 | 1e-9 | 1e-10 | 1e-12 |

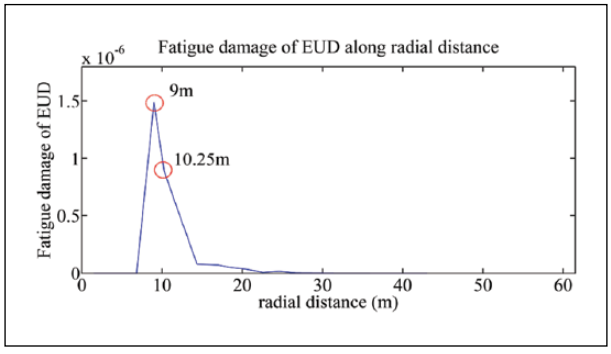


**Figure 11.** The illustration of EUD damage at different blade sections.

of one-dimensional beam model is presented based on Euler–Bernoulli assumption. To lower the order of derivative in governing equations, a transformation is proposed so that the variables are transformed from displacements to moments and vibration velocity. To begin with, the explicit method is employed to solve the beam equations with a simple formulation. In the next step, to break the limitation of time step in the explicit method, an implicit method is derived to solve the aforementioned beam equations. To recover the stress and strain time series from the moment and force time series of the EAL model, two-dimensional cross-sectional analysis method is employed. Based on the NREL 5MW baseline turbine blade data, several case studies are carried out to validate the EAL model and the fatigue damage of single turbine and

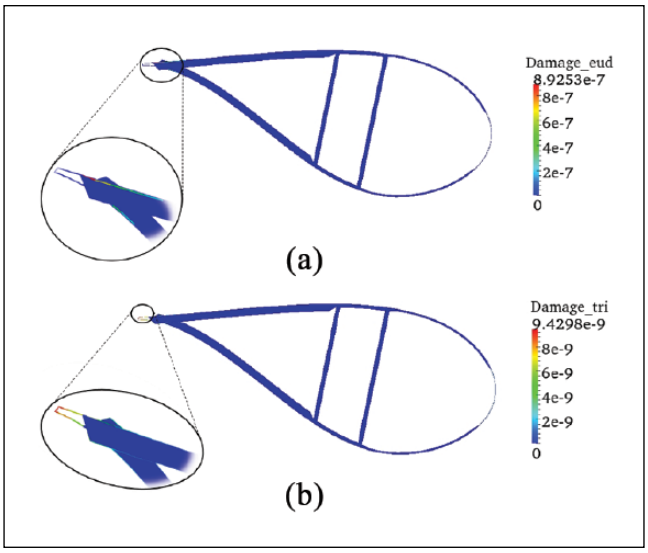


**Figure 12.** Fatigue damage critical zone illustration: (a) The fatigue damage of EUD at the critical section and (b) the fatigue damage of TRIAX at the critical section.

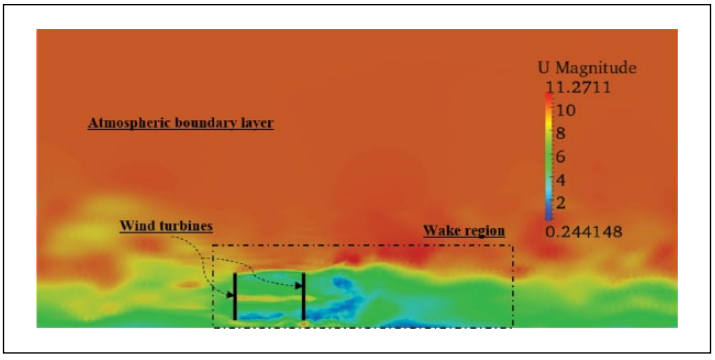


**Figure 13.** The illustration of wake flow for two in-a-line wind turbines.

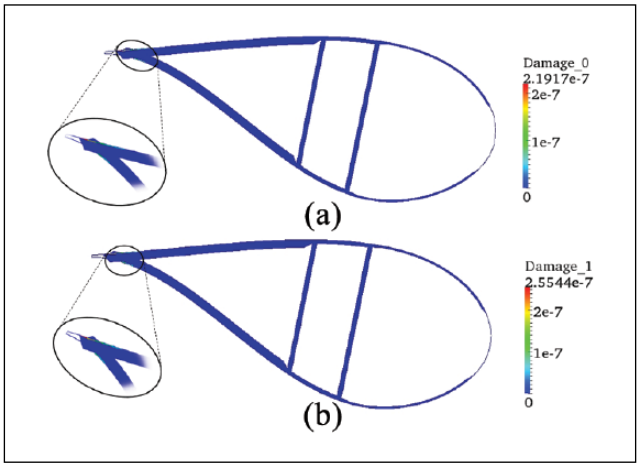


**Figure 14.** Comparison between upstream and downstream turbines in terms of fatigue damage of EUD: (a) The EUD fatigue damage of upstream turbine and (b) the EUD fatigue damage of downstream turbine.

two in-line turbines are calculated. The fatigue analysis provides information about fatigue damage of different materials, fatigue critical area and wake-induced fatigue, which are significantly important for wind turbine design and optimization and wind farm layout design. There are mainly three conclusions:

1. The explicit EAL and FAST agree with each other well in terms of bending moments under steady wind conditions. With a 10 times larger time step, results of the implicit EAL are almost the same as the explicit EAL. And the out-of-plane moment time series of implicit EAL and FAST have the same order of magnitude and low frequency fluctuations, and their in-plane moment time series coincide with each other. The calculated contours of fatigue damage at root obtainedwith both methods agree well with each other. However, the calculated fatigue damage of the EAL model is slightly lower than FAST.
2. Through the fatigue analysis along the blade by using EAL and two-dimensional sectional analysis method, EUD is determined to be the most vulnerable material with fatigue damage of around 1e-6 for our simulations, which is followed by TRIAX with 1e-9 fatigue damage. From the following detailed analysis, the largest fatigue damage occurs at the trailing edge of NREL 5MW turbine blade, and the fatigue critical section is at 10.25 m from root. The fatigue damage will cause the debonding of upper surface and lower surface of the blade, causing the whole blade to crack.
3. The wake-induced fatigue is found in the simulation of two in-line turbines with 200 m in between. From this simulation case, the wake will lead to 16% fatigue increase.

## Declaration of conflicting interests

The author(s) declared no potential conflicts of interest with respect to the research, authorship and/or publication of this article.

## Funding

The author(s) disclosed receipt of the following financial support for the research, authorship, and/or publication of this article: The work in this article is supported by the SHARCNET project 'Development of a multiscale modeling framework for short-term wind power forecasting' and China Scholarship Council (CSC).

## References

Barnes RH, Morozov EV and Shankar K (2015) Improved methodology for design of low wind speed specific wind turbine blades. *Composite Structures* 119: 677–684.

Bayo RT and Parro G (2015) Site suitability assessment with dynamic wake meandering model. A certification point of view. *Energy Procedia* 76: 177–186.

Blasques JP (2015) BECAS user's guide. DTU report, Risø DTU, Roskilde.

Blasques JP, Bitsche R, Fedorov V, et al. (2013) Applications of the beam cross section analysis software. In: *Proceedings of the 26th Nordic seminar on computational mechanics*, Oslo, 23 October, pp. 1–4. Available at: http://orbit.dtu.dk/fedora/objects/orbit:125116/datastreams/file_80226705-4861-44b8-9637-9131414940fa/content

Chen Z, Stol K and Mace B (2017) Wind turbine blade optimisation with individual pitch and trailing edge flap control. *Renewable Energy* 103: 750–765.

Churchfield MJ, Moriarty PJ, Hao Y, et al. (2015) A comparison of the dynamic wake meandering model, large-eddy simulation and field data at the Egmond aan Zee offshore wind plant. NREL report, NREL, Washington, DC.

Cortina G, Sharma V and Calaf M (2017) Investigation of the incoming wind vector for improved wind turbine yaw-adjustment under different atmospheric and wind farm conditions. *Renewable Energy* 101: 376–386.

Dahlberg JA, Poppen M and Thor SE (1992) Load/fatigue effects on a wind turbine generator in a wind farm 39: 199–209.

Frandsen ST, Chacon L, Crespo A, et al. (1996) Measurements on and modelling of offshore wind farms. *Riso Report* 903: 1169–1178.

Gaumond M, Réthoré P-E, Ott S, et al. (2014) Evaluation of the wind direction uncertainty and its impact on wake modelling at the Horns Rev offshore wind farm. *Wind Energy* 80: 1169–1178.

GL (2010) *Guideline for the Certification of Wind Turbines: Lloyd Rules and Guidelines, Industrial Services*. Oslo: GL.

Göçmen T, Laan PVD, Réthoré Pe Diaz AP, et al. (2016) Wind turbine wake models developed at the technical university of Denmark: A review. *Renewable and Sustainable Energy Reviews* 60: 752–769.

Jonkman JM and Buhl ML Jr (2005) *Fast User's Guide*. Washington, DC: NREL.

Kim SH, Shin HK, Joo YC, et al. (2015) A study of the wake effects on the wind characteristics and fatigue loads for the turbines in a wind farm. *Renewable Energy* 74: 536–543.

Lee S, Churchfield J, Moriarty PJ, et al. (2017a) A numerical study of atmospheric and wake turbulence impacts on wind turbine fatigue loadings. *Journal of Solar Energy Engineering* 135: 031001.

Lee K, Huque Z, Kommalapati R, et al. (2017b) Fluid-structure interaction analysis of NREL phase VI wind turbine: Aerodynamic force evaluation and structural analysis using FSI analysis. *Renewable Energy* 113: 512–531.

Miao W, Li C, Pavesi G, et al. (2017) Investigation of wake characteristics of a yawed HAWT and its impacts on the inline downstream wind turbine using unsteady CFD. *Journal of Wind Engineering & Industrial Aerodynamics* 168: 60–71.

Nedjari HD, Guerri O and Saighi M (2017) CFD wind turbines wake assessment in complex topography. *Energy Conversion and Management* 138: 224–236.
Pillai AC, Chick J, Khorasanchi M, et al. (2017) Application of an offshore wind farm layout optimization methodology at Middelgrunden wind farm. *Ocean Engineering* 139: 287–297.
Resor BR (2013) Definition of a 5mw/61.5m wind turbine blade reference model. Sandia report, Sandia National Laboratories, Albuquerque, NM; Livermore, CA.
Sørensen JN and Shen WZ (2002) Numerical modeling of wind turbine wakes. *Journal of Fluids Engineering* 124: 393–399.
Stäblein AR, Hansen MH and Pirrung G (2017) Fundamental aeroelastic properties of a bend–twist coupled blade section. *Journal of Fluids and Structures* 68: 72–89.
Thomsen K and Sørensen S (1999) Fatigue loads for wind turbines operating in wakes. *Journal of Wind Engineering and Industrial Aerodynamics* 80: 121–136.
Veers PS (1988) Three dimensional wind simulation. Sandia report, Sandia National Laboratories, Albuquerque, NM; Livermore, CA.
Vera-Tudela L and Kühn M (2017) Analysing wind turbine fatigue load prediction: The impact of wind farm flow conditions. *Renewable Energy* 107: 352–360.
Vermeer LJ, Sørensen JN and Crespo A (2003) Wind turbine wake aerodynamics. *Progress in Aerospace Sciences* 39: 467–510.
Vorpahl F, Strobel M, Jonkman JM, et al. (2014) Verification of aero-elastic offshore wind turbine design codes under IEA wind task XXIII. *Wind Energy* 17: 519–547.

## Appendix 1

The elements in parameter matrices for two-dimensional sectional model are listed in this appendix. All of these information is summarized from the BECAS tutorial. Most of the parameters are about surface integral of blade section

$$\underset{(6\times 6)}{\mathbf{A}} = \sum_{e=1}^{n_e} \int_A \mathbf{Z}_e^T \mathbf{S}_e^T \mathbf{Q}_e \mathbf{S}_e \mathbf{Z}_e dA \tag{44}$$

$$\underset{(n_d\times 6)}{\mathbf{R}} = \sum_{e=1}^{n_e} \int_A \mathbf{B}_e^T \mathbf{Q}_e \mathbf{S}_e \mathbf{Z}_e dA \tag{45}$$

$$\underset{(n_d\times n_d)}{\mathbf{E}} = \sum_{e=1}^{n_e} \int_A \mathbf{B}_e^T \mathbf{Q}_e \mathbf{B}_e dA \tag{46}$$

$$\underset{(n_d\times n_d)}{\mathbf{C}} = \sum_{e=1}^{n_e} \int_A \mathbf{B}_e^T \mathbf{Q}_e \mathbf{S}_e \mathbf{N}_{2d,e} dA \tag{47}$$

$$\underset{(6\times n_d)}{\mathbf{L}} = \sum_{e=1}^{n_e} \int_A \mathbf{Z}_e^T \mathbf{S}_e^T \mathbf{Q}_e \mathbf{S}_e \mathbf{N}_{2d,e} dA \tag{48}$$

$$\underset{(n_d\times n_d)}{\mathbf{M}} = \sum_{e=1}^{n_e} \int_A \mathbf{N}_{2d,e}^T \mathbf{S}_e^T \mathbf{Q}_e \mathbf{S}_e \mathbf{N}_{2d,e} dA \tag{49}$$

$$\underset{(n_d\times 6)}{\mathbf{D}} = \begin{bmatrix} \mathbf{I}_3 & \cdots & \mathbf{I}_3 \\ \mathbf{n}_1 & \cdots & \mathbf{n}_{n_n} \end{bmatrix}^T \tag{50}$$

In equation (50), $\mathbf{n}$ has the same form of the $\mathbf{n}_e$ in equation (53). And $\mathbf{I}_3$ is a unitary matrix. In those equations, $\mathbf{N}_{2d,e}$ is the two-dimensional shape function finite element on the cross section of the blade, which is four-node element in this study. $\mathbf{Q}_e$ is the elementary material constitutive matrix in Hooke's law, in which $\sigma_e = \mathbf{Q}_e \epsilon_e$ ( $\sigma_e$ is the elementary stress and $\epsilon_e$ is the elementary strain)

$$\mathbf{B}_e = \begin{bmatrix} \frac{\partial \square}{\partial x} & 0 & 0 \\ 0 & \frac{\partial \square}{\partial} & 0 \\ \frac{\partial \square}{\partial y} & \frac{\partial \square}{\partial x} & 0 \\ 0 & 0 & \frac{\partial \square}{\partial x} \\ 0 & 0 & \frac{\partial \square}{\partial y} \\ 0 & 0 & 0 \end{bmatrix} \tag{51}$$

$$\underset{(3\times 6)}{\mathbf{Z}_e} = \begin{bmatrix} \mathbf{I}_3 & \mathbf{n}_e \end{bmatrix} \tag{52}$$

$$\mathbf{n}_e = \begin{bmatrix} 0 & 0 & y \\ 0 & 0 & -x \\ -y & x & 0 \end{bmatrix} \tag{53}$$

$$\mathbf{S}_e = \begin{bmatrix} 0 & 0 & 0 \\ 0 & 0 & 0 \\ 0 & 0 & 0 \\ 1 & 0 & 0 \\ 0 & 1 & 0 \\ 0 & 0 & 1 \end{bmatrix} \tag{54}$$

$$\mathbf{T}_r = \begin{bmatrix} 0 & 0 & 0 & 0 & -1 & 0 \\ 0 & 0 & 0 & 0 & 1 & 0 \\ 0 & 0 & 0 & 0 & 0 & 0 \\ 0 & 0 & 0 & 0 & 0 & 0 \\ 0 & 0 & 0 & 0 & 0 & 0 \\ 0 & 0 & 0 & 0 & 0 & 0 \end{bmatrix} \tag{55}$$